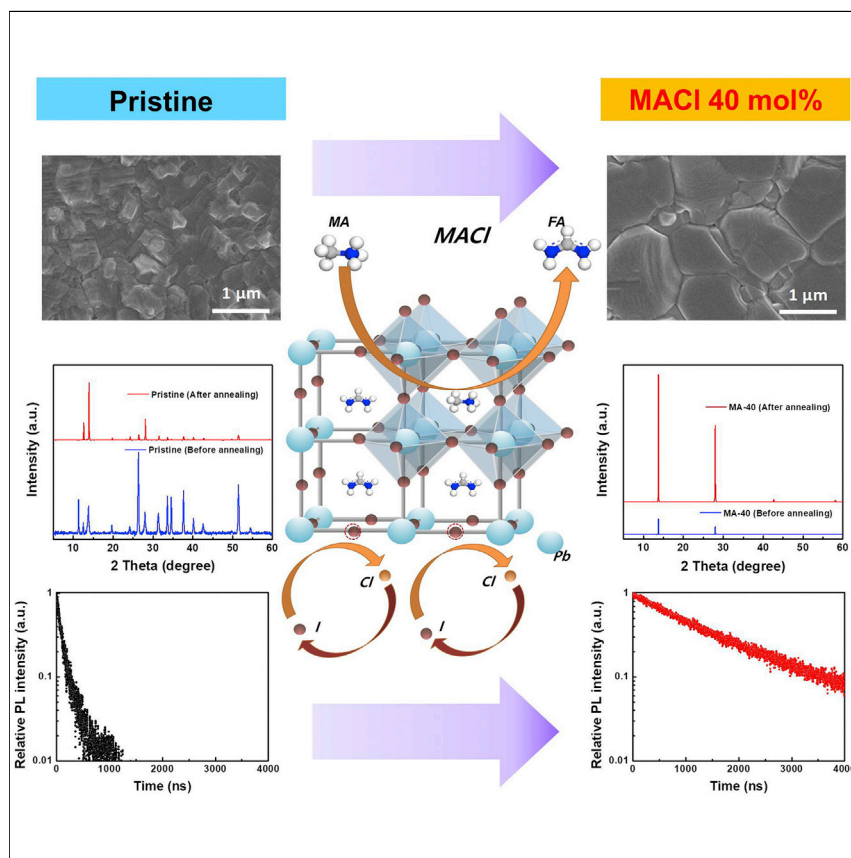


## Article

# Methylammonium Chloride Induces Intermediate Phase Stabilization for Efficient Perovskite Solar Cells



Kim and co-workers report systematical studies with methylammonium chloride (MACl) in formamidinium lead iodide ( $\text{FAPbI}_3$ )-based perovskite thin films. The MACl addition could induce the intermediate phase with pure  $\alpha$ -phase without annealing, effectively stabilizing the structure, only through cationic site substitution. The film quality can be significantly improved, exhibiting a  $6\times$  increase in grain size, a  $3\times$  increase in phase crystallinity, and a  $4.3\times$  increase in photoluminescence lifetime. The resulting optimized solar cells achieved a peak-scan efficiency of above 24%.

Minjin Kim, Gi-Hwan Kim, Tae Kyung Lee, ..., Sang Kyu Kwak, Jin Young Kim, Dong Suk Kim

skkwak@unist.ac.kr (S.K.K.)  
jykim@unist.ac.kr (J.Y.K.)  
kimds@kier.re.kr (D.S.K.)

## HIGHLIGHTS

Improvement of morphology, phase crystallinity, photo-physical property, and efficiency with MACl

Stabilized intermediate to the pure  $\text{FAPbI}_3$   $\alpha$ -phase with MACl

The formation energy of perovskite structure with the amount of incorporated MACl

Theoretical framework for understanding the interaction of MACl with a perovskite film



## Article

# Methylammonium Chloride Induces Intermediate Phase Stabilization for Efficient Perovskite Solar Cells

Minjin Kim,<sup>1,5,6</sup> Gi-Hwan Kim,<sup>2,6</sup> Tae Kyung Lee,<sup>4,6</sup> In Woo Choi,<sup>1</sup> Hye Won Choi,<sup>1</sup> Yimhyun Jo,<sup>1</sup> Yung Jin Yoon,<sup>3</sup> Jae Won Kim,<sup>3</sup> Jiyun Lee,<sup>4</sup> Dihong Huh,<sup>5</sup> Heon Lee,<sup>5</sup> Sang Kyu Kwak,<sup>4,\*</sup> Jin Young Kim,<sup>3,\*</sup> and Dong Suk Kim<sup>1,7,\*</sup>

## SUMMARY

One of the most effective methods to achieve high-performance perovskite solar cells has been to include additives that serve as dopants, crystallization agents, or passivate defect sites. Cl-based additives are among the most prevalent in literature, yet their exact role is still uncertain. In this work, we systematically study the function of methylammonium chloride (MACl) additive in formamidinium lead iodide ( $\text{FAPbI}_3$ )-based perovskite. Using density functional theory, we provide a theoretical framework for understanding the interaction of MACl with a perovskite. We show that MACl successfully induces an intermediate to the pure  $\text{FAPbI}_3$   $\alpha$ -phase without annealing. The formation energy is related to the amount of incorporated MACl. By tuning the incorporation of MACl, the perovskite film quality can be significantly improved, exhibiting a 6× increase in grain size, a 3× increase in phase crystallinity, and a 4.3× increase in photoluminescence lifetime. The optimized solar cells achieved a certified efficiency of 23.48%.

## INTRODUCTION

Within a short period of time, organic-inorganic lead halide perovskites have demonstrated powerful applications in solar cells as a result of high-power conversion efficiencies now exceeding 23%,<sup>1</sup> unprecedented in the field of photovoltaics. The high-efficiency outputs of perovskite solar cells are attributed to their exceptional material properties,<sup>2–4</sup> which include high optical absorption cross-sections,<sup>5</sup> low exciton binding energies,<sup>6</sup> long-range charge carrier diffusion lengths,<sup>3,7,8</sup> and easy tuning of the band gaps<sup>8–10</sup> via simple interchanges of the precursor components.

Among the perovskite materials, formamidinium lead iodide ( $\text{FAPbI}_3$ )-based perovskite materials are also widely used because the band gap, 1.48 eV, is closer to the optimum value of a single-junction solar cell<sup>11–13</sup> and displays a broader light absorption spectrum that extends to 840 nm, although stability can be an issue in these cells. In general,  $\text{FAPbI}_3$  has two crystal structures: a non-perovskite yellow  $\delta$ -phase and a 3D perovskite black  $\alpha$ -phase. Only the  $\alpha$ -phase perovskite is a useful photoactive phase.<sup>12,14</sup> Black  $\alpha$ -phase perovskite readily transforms to the yellow  $\delta$ -phase non-perovskite because of the large size of the FA cation.<sup>15</sup> Studies have shown that substituting some  $\text{FA}^+$  species with  $\text{MA}^+$  or  $\text{Cs}^+$  can inhibit this phase transformation.<sup>12</sup>

## Context & Scale

Numerous effective methods have been developed toward achieving high-performance perovskite solar cells. The additives are one of the most effective ways of achieving high performance. Cl-based additives are among the most prevalent in literature; however, their exact role is still uncertain.

Herein, we systematically researched the effects of methylammonium chloride (MACl) additive using analysis of photo-physical properties and density functional theory. The highest efficiency achieved was 24.02%, certified as 23.48%, and the resultant devices showed better thermal stabilities and photostabilities than the pristine devices.



The important factors for achieving high-performance perovskite solar cells include controlling the well-defined morphologies and maintaining the high crystallization of the perovskite film.<sup>16,17</sup> These features can be controlled through the choice of perovskite precursor,<sup>18</sup> fabrication method,<sup>19</sup> solvent mixing,<sup>17</sup> annealing conditions,<sup>20,21</sup> manufacturing humidity conditions,<sup>22</sup> surface passivation,<sup>23</sup> and processing additives.<sup>24</sup> Recently, the incorporation of additives into the perovskite precursor solution was widely studied to provide an effective approach to improving the film morphology and crystallinity. Several additives, including polymers,<sup>25–27</sup> fullerene derivatives,<sup>28–30</sup> organic halide salts,<sup>31–35</sup> metal halide salts,<sup>36–39</sup> inorganic acid,<sup>40–43</sup> and others<sup>44–46</sup> can be used to create a uniform perovskite layer with a high crystallinity and improve the device performance. Among these, additives containing iodide ions, such as cesium iodide (CsI),<sup>47–50</sup> rubidium iodide (RbI),<sup>51–53</sup> guanidinium iodide (Gul),<sup>54–56</sup> methylammonium iodide (MAI),<sup>57</sup> and other iodide<sup>58–61</sup> have driven the high-performance efficiencies. Just 5% or 10% CsI addition to perovskite mixtures suppressed non-perovskite yellow phase impurities and induced the formation of uniformly large perovskite grains that extended the electron-to-hole collecting layer, consistent with seed-assisted crystal growth.<sup>50</sup> Recently, alkali iodide (LiI, NaI, and KI) was used for defect engineering and perovskite doping to reduce hysteresis and increase efficiencies using small doping concentrations of 10 µmol.<sup>62</sup>

Apart from the cationic iodide additives, chloride-based additives have been studied recently, although few studies have compared the chlorides with the iodides. Wang et al. explored the additions of FACL and MACl in equal molar amounts to the FAPbI<sub>3</sub> precursor solution, demonstrating that they were good additives for increasing the crystallization of α-FAPbI<sub>3</sub> via the formation of intermediate mixtures, which suppressed crystallization of the δ-phase FAPbI<sub>3</sub>.<sup>63</sup> A new perovskite growth method was presented using MACl to assist the vertical recrystallization in an FA perovskite film and provide an efficiency of 20.6%.<sup>64</sup> Mu et al. showed that MACl was a transitional “stabilizer” that preserved the crystal structure and formed the black FA perovskite.<sup>65</sup> Qing et al. also showed that the synergistic effects of dimethyl sulfoxide (DMSO) and MACl additives, which assisted crystallization of the perovskites, lead to a single-crystal-like film with a smooth surface and a low defect density, thereby providing a high-efficiency perovskite solar cell.<sup>66</sup> However, the efficiencies of the perovskite solar cells prepared with cationic chloride additives were lower than those prepared using cationic iodide additives. Furthermore, it is not yet clear why MACl additives would be better than others. This effect requires further investigation of the role and theoretical calculation.

In this work, we systematically studied the role of MACl additive in FAPbI<sub>3</sub>-based perovskite solar cells. The grain size in films prepared using various contents was dramatically greater, by a factor of 6, compared to the film prepared without additive. Interestingly, MACl effectively stabilizes an intermediate to the pure FAPbI<sub>3</sub> α-phase without annealing—only through cationic site substitution. From the fabricating high crystallinity of ultra-pure α-phase FAPbI<sub>3</sub>-based perovskite, the photoluminescence lifetimes also increased by a factor of 4.3. Using density functional theory (DFT), we provide a theoretical framework for understanding the interaction of MACl with a perovskite active layer. The formation energy of the resulting perovskite structure is related to the amount of incorporated MACl. Consequently, MACl additive induces intermediate phase stabilization for over 24% efficiency. The highest efficiency achieved was 24.02%, which was obtained with the addition of 40 mol% MACl. These results suggest that the MACl additive is a promising material for high-quality film formation and high-performance device that offers great opportunities for the practical applications.

<sup>1</sup>KIER-UNIST Advanced Center for Energy, Korea Institute of Energy Research (KIER), UNIST-Gil 50, Eonyang-eup, Ulju-gun, Ulsan 689-851, Republic of Korea

<sup>2</sup>Photonic Energy Research Center, Korea Photonics Technology Institute (KOPTI), Gwangju 500-779, Republic of Korea

<sup>3</sup>Perovtronic Research Center, Department of Energy Engineering, Ulsan National Institute of Science and Technology (UNIST), UNIST-Gil 50, Eonyang-eup, Ulju-gun, Ulsan 689-851, Republic of Korea

<sup>4</sup>Department of Energy Engineering, School of Energy and Chemical Engineering, Ulsan National Institute of Science and Technology (UNIST), UNIST-Gil 50, Eonyang-eup, Ulju-gun, Ulsan 689-851, Republic of Korea

<sup>5</sup>Department of Materials and Science Engineering, Korea University, 5-1 Anam-dong, Sungbuk-Gu, Seoul 136-701, Republic of Korea

<sup>6</sup>These authors contributed equally

<sup>7</sup>Lead Contact

\*Correspondence: [skkwak@unist.ac.kr](mailto:skkwak@unist.ac.kr) (S.K.K.), [jykim@unist.ac.kr](mailto:jykim@unist.ac.kr) (J.Y.K.), [kimds@kier.re.kr](mailto:kimds@kier.re.kr) (D.S.K.)

<https://doi.org/10.1016/j.joule.2019.06.014>

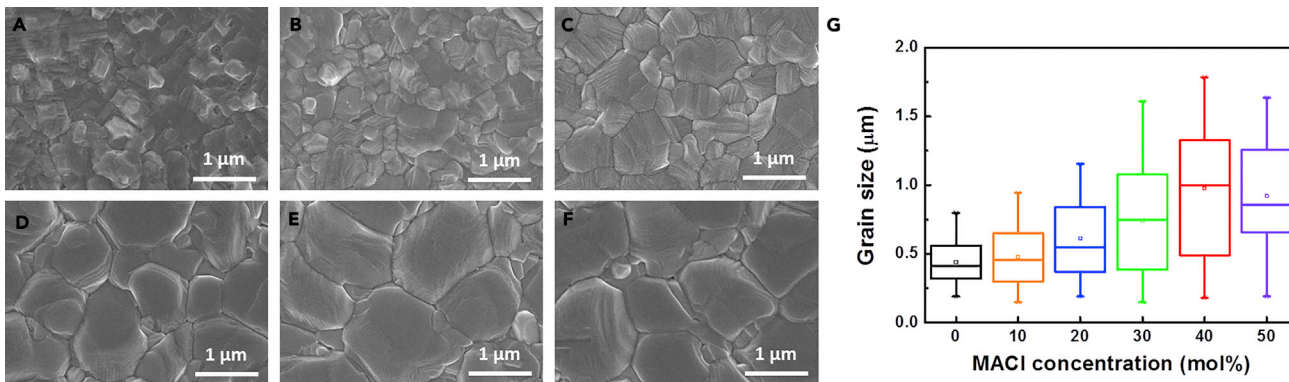


**Figure 1. SEM Images and Grain Size Distribution of Perovskite Films**

(A–F) Top view of SEM images of devices prepared with different amounts of MACl: (A) pristine (without addition), (B) MA-10, (C) MA-20, (D) MA-30, (E) MA-40, and (F) MA-50.

(G) Grain size distribution of the films as a function of the MACl contents (pristine, MA-10, MA-20, MA-30, MA-40, and MA-50). Note that for the results of grain size distribution, all grains are measured.

## RESULTS AND DISCUSSION

The surface morphologies of the different film compositions were evaluated by collecting top-view images using a scanning electron microscope (SEM). The interesting results were that the grain sizes of perovskite films are directly related to the amount of incorporated MACl. Figure 1A shows the photographs of the film surfaces manufactured using the MACl introduced in concentrations of 10 mol%, 20 mol%, 30 mol%, 40 mol%, and 50 mol% (denoted MA-10, MA-20, MA-30, MA-40, and MA-50, respectively). The grain size obtained without the additive (pristine) was approximately 250 nm (average). However, the MA-10 produced a film with a larger grain size of 600 nm (see Figure 1B). The grain size obtained from the MA-20 was 1,000 nm, and the grain size further increased to 1,500 nm for the MA-40 (see Figures 1C–F). The grain size distributions obtained with different additions of MACl contents is shown in Figure 1G. Atomic force microscopy (AFM) phase images (Figure S1) also showed that the grain sizes were increased as a function of the additive amounts. The film roughness was measured by calculating the root-mean-square (RMS) roughness as listed in Table S1. The pristine film consisted of small crystals with an RMS roughness of 64.7 nm. The roughness decreased to 45.8 nm, 41.0 nm, 33.6 nm, and 24.7 nm with MA-10, MA-20, MA-30, and MA-40, respectively. These results indicated that the film roughness was reduced when the MACl contents were increased.

To check the substitution of the cationic site with MA ion and anionic site with Cl ion, the perovskite films were characterized elementally using X-ray photoelectron spectroscopy (XPS), as shown in Figure S2. The intensity of nitrogen (N) peak decreased with the MACl contents, indicating that the MA ion was substituted for FA in the cationic site because the MA ion included one N atom and the FA ion included two N atoms. Therefore, if the FA ion had been substituted by MA ions, the intensity of N would decrease as the MACl addition increased. In contrast with the N ion, the Cl ion was not substituted into the anionic sites. Some studies have shown that the addition of Cl ions to a perovskite does not facilitate the formation of a continuous perovskite phase because Cl ions readily evaporate away during the annealing process.<sup>63,65</sup> To evaluate the Cl ion content, XPS measurements of the Cl ions were conducted as a function of the MACl contents from MA-10, MA-30, and MA-50. As shown in Figure S2B, the signal corresponding to the Cl ion content in the film was not detected in all samples. These results indicated that the Cl ion had

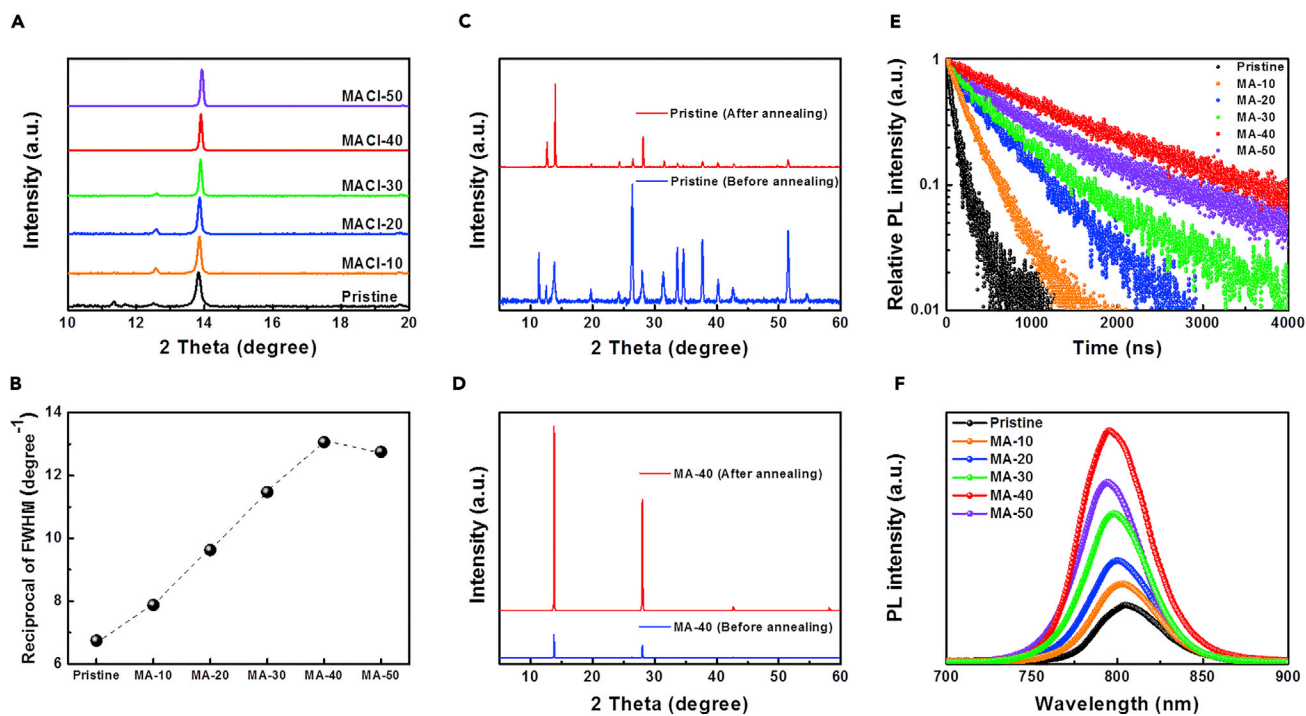


**Figure 2. XRD Spectra and Photoluminescence Data of Perovskite Films**

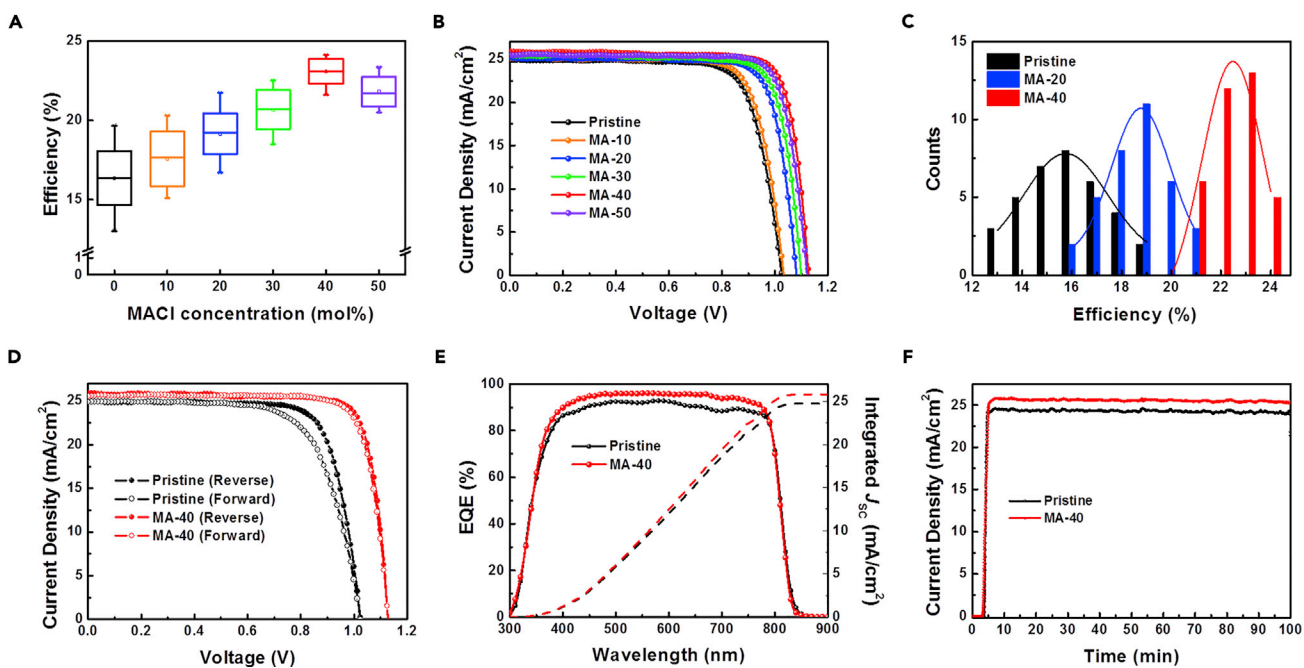
- (A) XRD spectra of perovskite films prepared with different amounts: pristine, MA-10, MA-20, MA-30, MA-40, and MA-50.
- (B) Reciprocal FWHM obtained from films prepared with different additive concentrations at the diffraction peak 13.9° for the  $\alpha$ -phase perovskite.
- (C) XRD data obtained from perovskite films prepared without MACI before and after annealing at 150°C for 10 min.
- (D) XRD data obtained from perovskite films prepared with MA-40 before and after annealing at 150°C for 10 min.
- (E) TRPL decay profiles of the perovskite films prepared with pristine, MA-10, MA-20, MA-30, MA-40, and MA-50.
- (F) Steady-state photoluminescence spectra of perovskite films prepared with pristine, MA-10, MA-20, MA-30, MA-40, and MA-50.

evaporated during annealing. MACI easily decomposed into MA ion and  $\text{FACl}$ , which was easily removed from the film through evaporation with annealing.<sup>65</sup> To support this result, the Cl ion was monitored using energy dispersive spectroscopy (EDS) analysis to observe any changes in the Cl ion concentration during annealing. The results shown in Figure S3 reveal a large initial amount of Cl present compared to the amount of Pb (Cl/Pb atomic ratio) present in a perovskite film not subjected to annealing. After annealing at 150°C for 5 min, the Cl ion content was reduced to a 0.12 Cl/Pb atomic ratio, and no EDS-detectable Cl ion was observed in the perovskite film after annealing at 150°C for 10 min. These results agree with the XPS analysis. The intensities of the Pb and I ion signals did not change, indicating that the halide mixture composition did not change.

Another interesting result is that the crystallinity can be changed with different concentrations of MACI. Figure 2A shows the diffractograms obtained from pristine, MA-10, MA-20, MA-30, MA-40, and MA-50, respectively. The pristine perovskite film (prepared without additive) showed peaks at 12.7° and 13.9°, corresponding to the  $\text{PbI}_2$  and  $\alpha$ -phase perovskite peaks. The small  $\text{PbI}_2$  peak intensity indicated that the film was not fully converted into a pure  $\alpha$ -phase perovskite film during annealing at 150°C for 10 min. The crystallinity with addition of MACI, in MA-10, MA-20, and MA-30, slightly increased the  $\alpha$ -phase peak at 13.9°, and the  $\text{PbI}_2$  peak at 12.7° disappeared. The  $\alpha$ -phase perovskite peak further increased at MA-40. However, the intensity of  $\alpha$ -phase peak is slightly decreased at MA-50. The film crystallinities obtained from different MACI contents were compared by

plotting the reciprocal full width at half maximum (FWHM) from the XRD spectra as shown in [Figure 2B](#). The FWHM values were compared under the best conditions for each additive: pristine, MA-10, MA-20, MA-30, MA-40, and MA-50. The narrower diffraction peaks were observed in the films prepared with additive as compared to the pristine film. The highest value was obtained from MA-40, which indicated that large crystallites could be obtained. These results agreed with the grain size results, as shown in [Figure 1](#). The very interesting result is that MACl successfully induces an intermediate to the pure FAPbI<sub>3</sub>  $\alpha$ -phase without annealing, effectively stabilizing this structure. The pristine film, for example, prepared without additives and without annealing, displayed numerous unknown diffraction peaks, as shown in [Figure 2C](#). After annealing at 150°C for 10 min, the peak corresponding to the  $\alpha$ -phase perovskite was dominant, but some  $\delta$ -phase and PbI<sub>2</sub> were still present, indicating that it was not easy to obtain only ultra-pure  $\alpha$ -phase perovskite film from a pristine perovskite precursor solution. However, the perovskite film, obtained using MA-40, featured only a pure  $\alpha$ -phase perovskite peak (no detectable  $\delta$ -phase and PbI<sub>2</sub>) even without annealing ([Figure 2D](#)). After annealing at 150°C for 10 min, the peak corresponding to the  $\alpha$ -phase perovskite was sharply increased with only ultra-pure structure. These results indicate that the MACl additive can influence the formation of  $\alpha$ -phase structure even before the annealing step and that the stabilized intermediate can be induced into the ultra-pure  $\alpha$ -phase perovskite after the annealing step. To see the intermediate phase of FAPbI<sub>3</sub> perovskite with MACl addition more clearly, we measured the XRD of FAPbI<sub>3</sub> perovskite included with MA-40 according to the annealing time ([Figure S4](#)) and magnified the peak position around 14° ([Figure S5](#)). As expected, the peak position was slightly shifted to a smaller degree as the annealing time was increased, which indicated that the Cl ion was substituted by I ion during the annealing process ([Figures S2 and S3](#)). The photophysical measurements were conducted from the perovskite films prepared with different additive contents. Time-resolved photoluminescence (TRPL) decay profiles were obtained from the perovskite films. The PL decay curves, measured at the peak emission (800 nm), showed bi-exponential decays with a fast ( $\tau_1$ ) and a slow ( $\tau_2$ ) component. The  $\tau_1$  decay component corresponded to non-radiative recombination from defects (surface traps near the grain boundaries), and the  $\tau_2$  component corresponded to radiative recombination from the bulk perovskite.<sup>57</sup> [Figure 2E](#) plots the PL decay curves obtained from the different concentrations of the MACl addition. The pristine film provided  $\tau_1$  (331 ns) and  $\tau_2$  (68.7 ns), but the highest values were obtained at MA-40: 1,441 ns ( $\tau_1$ ) and 450 ns ( $\tau_2$ ), as shown in [Table S2](#). The higher decay values indicated that the deposited perovskite films possessed larger numbers of carriers after 1,000 ns, attributed to the strong suppression of non-radiative recombination. Longer components suggest improved Schottky order in the bulk perovskite as a result of additives.<sup>57</sup> Steady-state PL measurements were collected from the perovskite films deposited on glass. The corresponding curves for all compositions are shown in [Figure 2F](#). The intensities of the PL peaks gradually increased with the MACl contents, and a slight blue shift was observed in the emission peak due to the MA ion substitution. As discussed above, the PL was only slightly affected if only the cations were substituted, in agreement with the smaller observed shift in the band gap.<sup>67</sup> The highest PL intensities were found in MA-40, indicating a high crystal quality, in agreement with the XRD results.

The solar cell efficiencies with different concentrations were investigated, and the results are summarized in [Figure 3A](#) and [Table S3](#). The efficiency prepared with pristine was lower than the MA-10 and MA-20 devices. It was reasonable to assume that lower crystallinity of  $\alpha$ -phase perovskite dominated the films prepared with MA-10 and MA-20. The performances of devices prepared with MACl-30 improved, to an

**Figure 3. Photovoltaic Performance Characteristics**

- (A) Efficiency distribution of perovskite solar cells with different amounts of MACI.
- (B) Device performance current density-voltage ( $J$ - $V$ ) curves of perovskite devices with pristine, MA-10, MA-20, MA-30, MA-40, and MA-50.
- (C) Comparison of distribution efficiencies for pristine, MA-20, and MA-40 devices.
- (D)  $J$ - $V$  curves of reversed and forward scans for the MA-40 and pristine devices.
- (E) EQE spectra for the MA-40 and pristine devices.
- (F) Photocurrent density measured at the maximum power point of a 100 min span.

efficiency of 22.52%, further increased to 24.02% (MA-40), and slightly decreased to 23.36% with further addition (MA-50). These result trends agreed with the XRD, optical adsorption, and PL measurements discussed above. Larger grain size, better crystallinity, and higher absorption intensities gave rise to better performance efficiencies. The intensity of the absorption band was highest at MA-40, and the PL lifetimes were also maximized. The reliability of the efficiency results was determined by testing the devices at an external institute, as shown in Figure S6. The certified efficiency of 23.48% from Newport Corp. was obtained. Figure 3B shows the  $J$ - $V$  curves as a function of the MACI contents. The relative distribution efficiencies of the pristine film, MA-20, and MA-40 are also shown in Figure 3C. The current densities were found to be  $24.99 \text{ mA cm}^{-2}$  (MA-10),  $25.23 \text{ mA cm}^{-2}$  (MA-20),  $25.45 \text{ mA cm}^{-2}$  (MA-30),  $25.92 \text{ mA cm}^{-2}$  (MA-40), and  $25.38 \text{ mA cm}^{-2}$  (MA-50), better than the current density measured from the pristine perovskite,  $24.84 \text{ mA cm}^{-2}$ . It may be postulated that the current densities were also affected by the perovskite crystallinity. The higher crystallinity had the higher current density, which was consistent with UV-absorption spectra as shown in Figure S7. The large  $\text{PbI}_2$  peak observed in the pristine perovskite film indicated that the pristine perovskite film was not fully converted into a pure  $\alpha$ -phase perovskite film. Apart from the current density,  $V_{oc}$  significantly differ according to the different additives. The  $V_{oc}$  of a pristine device was  $1.027 \text{ V}$ , but higher values were obtained with the MA-10 ( $1.034 \text{ V}$ ), MA-20 ( $1.083 \text{ V}$ ), MA-30 ( $1.101 \text{ V}$ ), MA-40 ( $1.130 \text{ V}$ ), or MA-50 ( $1.123 \text{ V}$ ). The  $V_{oc}$  depends on the recombination rate in the perovskite film. The efficiencies obtained from the FACL and MAI additives were also measured by fabricating the various devices using the procedures described above, and the resulting  $J$ - $V$  curve efficiencies are

shown in [Figures S8](#) and [S9](#). The cell efficiencies obtained with FACL additive were higher than those of pristine, but the MAI additions were lower than those obtained from the cationic chloride addition at all concentrations. These results suggested that the chloride ion significantly affected the device performance. [Figure 3D](#) showed the J-V curve of reverse and forward scan for the best and pristine devices. A pure perovskite film has a slow recombination rate. The case of MA-40 had a longer lifetime and a strong PL intensity (see [Figures 2E](#) and [2F](#)) compared to pristine and other additive devices, which was a major contributor to higher  $V_{oc}$  values. The FF also has higher value at MA-40, but the difference of FF is smaller compared to the other values ([Figure 3B](#)). [Figure 3E](#) shows the external quantum efficiency (EQE) values and its integrated  $J_{sc}$  of pristine and best devices. The EQE spectra show that the average EQE is well matched with each current density. Because of substituting MA ion, the EQE spectra also can be slightly shifted with shorter wavelength as shown in [Figure S10](#). [Figure 3F](#) shows the stabilized steady-state current measured at the maximum power point (at 0.98 V) over 100 min.

Although inorganic-organic hybrid perovskites have displayed dramatic advances in photovoltaic applications, overcoming instabilities against light, heat, and moisture remains a challenge in the development of commercial applications. Device stability tests were conducted under room temperature (RT) and 40°C, and photo stabilities were conducted under constant AM 1.5G illumination at 25% relative humidity (RH) and without encapsulation. The stability at RT showed 90% retaining of its initial performance over 1,200 h as shown in [Figure S11A](#). The 40°C thermal stability test showed that the pristine device degraded to 60% of its initial performance over 300 h, but the MA-40 were more stable, retaining 90% of its initial performances ([Figure S11B](#)). The photostabilities of the pristine and MA-40 devices also give higher stability in conditions of continuous illumination, as shown in [Figure S11C](#). The improved stability against thermal and light illumination was attributed to the large grain size and high crystallinity of the perovskite films. Perovskite degradation appears to initiate at grain boundaries and surface defects upon exposure to moisture or constant light.<sup>68</sup> The grain size in the MA-40 film was almost 1,000 nm (average), 2.7 times the value of the pristine film (370 nm [average]; see [Figure 1A](#)). Therefore, degradation at the grain boundary sites in large-grain films was lower than in small-grain films. The MA-40 device was more stable than the pristine device. An additional factor supporting the improved thermal and photostability was the high film crystallinity. As shown in the XRD analysis, the film prepared with MA-40 displayed a higher crystallinity in the  $\alpha$ -phase perovskite crystal, as shown in [Figures 2A](#) and [2B](#). The higher crystallinity of the film reduced surface defects capable of reacting and degrading the material. Therefore, the MA-40 device displayed a strong stability against thermal and light illumination.

The mechanism by which cationic chloride improved the physical properties and efficiencies of the perovskite films was studied by using the DFT calculations (see [Experimental Procedures](#)). In view of the factors and experimental observations, we investigated the role of MACl additive on the perovskite crystal structure from three important points of view: roles of Cl and MA and concentration effect of MACl on the  $\alpha$ -phase  $\text{FAPbI}_3$  perovskite structure. First, to understand the role of Cl on the perovskite crystal structure, the formation energies of the  $\alpha$ -phase  $\text{FAPbI}_3$  perovskite structure and that including Cl, MA, or MACl were calculated ([Figure 4A](#)) from model systems ([Figures S12](#) and [S13](#)). The formation energies revealed that Cl stabilized the perovskite structure thermodynamically compared to the system without Cl. To better understand the role of Cl in electronic properties, the highest-occupied molecular orbital (HOMO) was calculated ([Figure 4B](#)). It has been

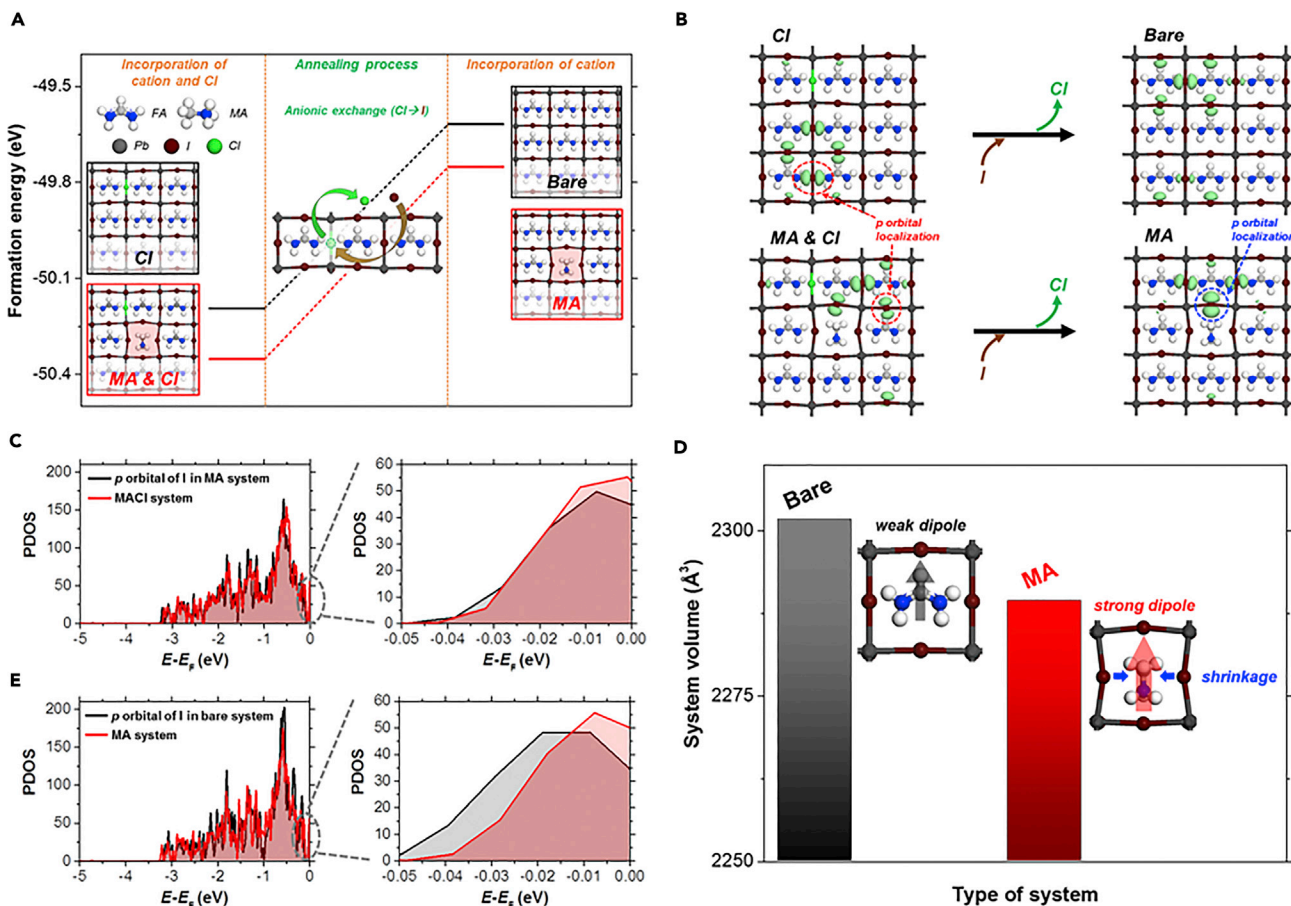


**Figure 4. Theoretical Calculation for the Role of MACl Additive on the  $\alpha$ -Phase FAPbI<sub>3</sub> Perovskite Structure**

(A and B) Calculations of the  $\alpha$ -phase FAPbI<sub>3</sub> perovskite structure and that prepared with Cl, MA, or MACl. Formation energies (A) and highest-occupied molecular orbitals (HOMOs) (B) of bare  $\alpha$ -phase FAPbI<sub>3</sub> perovskite structure and that with Cl, MA, or MACl. Note that the isosurface value of the HOMO was 0.01 e/Å<sup>3</sup>. The red and blue dashed circles indicate  $p$  orbital localization on I.

(C) Projected density of states (PDOS) of the perovskite system including MA or MACl. Note that for the system including MA, the  $p$  orbital of I is considered except for one I, which occupies the Cl site in the system including the MACl.

(D) Total volume and cubo-octahedral structure of the bare  $\alpha$ -phase FAPbI<sub>3</sub> perovskite structure and that prepared with MA.

(E) PDOS of the bare  $\alpha$ -phase FAPbI<sub>3</sub> perovskite structure and that prepared with MA.

reported that the FA interacts weakly with the I of perovskite structure with a cubo-octahedral structure favored by Pb and I in the  $\alpha$ -phase FAPbI<sub>3</sub>, resulting in an unstable perovskite structure.<sup>48</sup> Interestingly, Cl induced  $p$  orbital localization of I (red dashed circle in the Figure 4B), and the projected density of states (PDOS) results revealed that Cl enhanced the intensity of the  $p$  orbital of I at the HOMO state (Figures 4C and S14). Accordingly, the interactions of FA and I could be enhanced by the above-mentioned effects of Cl, which contributes to improving the stability of the FAPbI<sub>3</sub> perovskite structure. These results can be supported by the XRD and XPS results (Figures 2D and S2).

Second, we investigated the effects of MA cation incorporated into the perovskite structure. Lee et al. reported that the incorporation of the Cs cation at the FA site improved the stability of the perovskite by enhancing interactions between FA and I through shrinkage of the cubo-octahedral volume.<sup>48</sup> Based on this observation, we also confirmed the total volume shrinkage in the MA cation-incorporated system (i.e., ~0.57%) compared to the bare  $\alpha$ -phase FAPbI<sub>3</sub> perovskite system

(Figure 4D). The main contribution for this volume shrinkage is attributed to the contraction of MA-included cubo-octahedral site compared to the bare system (i.e., ~0.89%) (Figure S15). Moreover, we predicted that the dipole effect of the MA cation was another factor of lower formation energy of the MA system (Figure 4A) because the MA cation had a dipole moment 10 times that of the FA cation.<sup>69</sup> Our calculations indicated that  $p$  orbital localization of I in the MA system resulted from the dipole effect of the MA cation (blue dashed circle in Figure 4B). The PDOS of the MA cation-incorporated system revealed that the intensity of the  $p$  orbital of I in the HOMO state was higher than the bare  $\alpha$ -phase FAPbI<sub>3</sub> perovskite structure (Figure 4E). Therefore, we conclude that the effects of the volume shrinkage and the dipole enhance the interactions between FA and I, which improved the stability of the perovskite structure. We additionally investigated the volume shrinkage of perovskite structure in terms of the MA concentration. For this investigation, the four concentration systems were constructed (Figure S16). It was found that the volume shrinkage increased as the concentration of MA increased from calculation and experiment results. The degree of the volume shrinkage from both methods agreed well with each other (Figure S17). Thus, we confirmed that MA induced the volume shrinkage of the perovskite structure and its concentration influenced the degree of volume shrinkage.

Third, to elucidate the appropriate concentration of MACl additive for obtaining high crystallinity of  $\alpha$ -phase FAPbI<sub>3</sub> perovskite structure, the concentration effect of MACl was investigated. Based on the four concentration systems in Figure S16, we predicted that the optimal concentration ranges for high crystallinity of perovskite solar cell could exist and be elucidated by considering formation energy (Figure S13) and doping formation energy (Figure S18). Our theoretical prediction was in good agreement with experimental observation. In Figure S19, the optimal concentration of MACl was caused by the doping formation energy of MACl into the  $\alpha$ -phase FAPbI<sub>3</sub> perovskite structure in the pre-annealing step and the formation energy of the perovskite structure including MAI in the post-annealing step. Especially, the formation energy was stabilized between 33% and 44%, which corresponded to the best performance shown in the experiment (i.e., 40%). These theoretical predictions were in good agreement with experimental observations of results of the J-V curve (Figure 3B and Table S3). Overall, from the three points of DFT calculation, we can understand why MACl additive stabilized the perovskite formation and showed high performance.

## Conclusion

In summary, we investigated the MACl effects in the perovskite films, which construct the intermediate-phase into the perovskite film for the high-quality pure  $\alpha$ -phase perovskite film. With achieved high-quality pure  $\alpha$ -phase perovskite film, the surface morphology, crystallographic properties, optical absorption, and photoluminescence properties were enhanced, which resulted in high-performance perovskite solar cells. We achieved 24.02% perovskite solar cell performance. The mechanism of MACl's effect on the formation of  $\alpha$ -phase perovskite structure was elucidated using DFT calculation. We believe that our new finding will help researchers to achieve high performance of perovskite solar cells.

## EXPERIMENTAL PROCEDURES

### Materials

Formamidine acetate salt (99%), hydriodic acid (HI, 57 wt% in water), titanium diisopropoxide bis(acetylacetone), 2-propanol (anhydrous, 99.5%), chlorobenzene (anhydrous, 99.8%), N,N-dimethylformamide (DMF, anhydrous 99.8%,), and dimethyl

sulfoxide (DMSO, > 99.5%) were procured from Sigma-Aldrich and used as received. Methylamine hydrochloride (MACl, 98%) was procured from Acros Organics. Fluorine-doped tin oxide on glass (FTO glass,  $7 \Omega \text{ sq}^{-1}$ ) was obtained from Asahi. Ethanol (absolute, 99.9%) was procured from Changshu Yangyuan Chemicals. Diethyl ether (extra pure grade) was procured from Duksan. TiO<sub>2</sub> paste (SC-HT040) was purchased from ShareChem. Lead iodide (PbI<sub>2</sub>, 99.999%) was purchased from TCI.

### Materials Synthesis

Formamidinium iodide (FAI) was synthesized as reported elsewhere.<sup>70</sup> Briefly, 25 g formamidinium acetate was directly mixed with 50 mL hydriodic acid in a 500 mL round-bottomed flask with vigorous stirring. A light yellow powder was obtained by evaporating solvent at 80°C for 1 h in a vacuum evaporator. The resulting powders were dissolved in ethanol and precipitated using diethyl ether. This procedure was repeated 3 times until white powders were obtained, and the powders were recrystallized from ethanol and diethyl ether in a refrigerator. After recrystallization, the resulting powders were collected and dried at 60°C for 24 h. Single-crystal FAPbI<sub>3</sub> was fabricated as reported previously.<sup>71,72</sup>

### Device Fabrication

Asahi FTO glass (FTO glass,  $7 \Omega \text{ sq}^{-1}$ ) was used as the substrate for the devices. The substrates were cleaned using the RCA-2 (H<sub>2</sub>O<sub>2</sub>-NCl-H<sub>2</sub>O) procedure<sup>73</sup> for 15 min to remove metal ion impurities. The substrates were then cleaned sequentially with acetone, ethanol, and isopropyl alcohol (IPA) in an ultrasonic system for 15 min. To deposit the compact TiO<sub>2</sub> layer, 60 mL of a titanium diisopropoxide bis(acetylacetone)/ethanol (with 1:10 volume ratio) solution was applied by spraying. Prior to spraying, the substrates were placed on a hot plate and the temperature was increased to 450°C rapidly. After completing the spray pyrolysis step, the substrates were stored at 450°C for 1 h to improve the electrical properties,<sup>74</sup> then slowly cooled to room temperature. On top of the c-TiO<sub>2</sub> layer, a mesoporous TiO<sub>2</sub> (mp-TiO<sub>2</sub>) layer was deposited by spin-coating. The TiO<sub>2</sub> paste, approximately 50 nm in diameter, was purchased from ShareChem. The paste was dispersed in ethanol/terpineol (78:22 w/w). The FTO/c-TiO<sub>2</sub> substrates prepared with mp-TiO<sub>2</sub> were heated at 500°C on a hot plate for 1 h to remove organic compounds and then slowly cooled to 200°C. To fabricate perovskite solar cells, the perovskite precursor solution was prepared by mixing 1,139 mg mL<sup>-1</sup> FAPbI<sub>3</sub> in a mixture of DMF and DMSO in a 4:1 ratio by volume. MACl was added in the range 0~50 mol%. For each sample, 70 μL of the filtered solution was spread over the FTO/c-TiO<sub>2</sub>/mp-TiO<sub>2</sub> substrate at 6,000 rpm for 50 s with 0.1 s ramping. During spin coating, 1 mL diethyl ether was dripped after spinning for 10 s using a pipette. The film was dried on a hot plate at 150°C for 10 min. After cooling the substrate, the perovskite film was spin coated with phenylethylammonium iodide (PEAI) dissolved with IPA (5 mM) at 3,000 rpm. The hole transfer materials were deposited by preparing a spiro-OMe-TAD (Lumtech) in chlorobenzene (90 mg/mL) and mixing with 35.5 μL 4-tert-butylpyridine (TBP), 23 μL Li-bis(trifluoromethanesulfonyl)imide (Li-TFSI) (520 mg/mL acetonitrile), and 5 μL tris(2-(1-h-pyrazol-1-yl)-4-tert-butylpyridine)-cobalt(III)tris(bis(trifluoromethylsulfonyl)imide) (FK209, Lumtech) (180 mg/mL acetonitrile). Finally, a gold counter electrode was deposited on the substrate using a thermal evaporation system. The back and front contacts were formed from 100 nm thick Au films deposited by vapor deposition at a pressure of 10<sup>-6</sup> torr.

### Characterization

The phases of the perovskite films prepared with different additives were analyzed using X-ray diffractometry (XRD) using a D8 Advance (Bruker) diffractometer

equipped with Cu K $\alpha$  radiation ( $\lambda = 0.1542$  nm). The morphologies of the perovskite films were assessed using a field-emission scanning electron microscope (FE-SEM, S-4800, Hitachi). Steady-state photoluminescence and TRPL measurements were conducted using PicoQuant FluoTime 300 (PicoQuant GmbH, Germany) equipped with a PDL 820 laser pulse driver. A pulsed laser diode ( $\lambda = 375$  nm, pulse FWHM < 70 ps, repetition rate 200 kHz–40 MHz) was used to excite the sample. XPS spectra were collected using a Thermo Fisher Scientific ESCALAB 250XI at a base pressure of  $1.0 \times 10^{-9}$  torr using a monochromatic Al-K $\alpha$  X-ray source. The solar cells were measured using a solar simulator (McScience, K3000 Lab solar cell I-V measurement system, Class AAA) at  $100\text{ mA cm}^{-2}$ , illumination AM 1.5 G. The light intensity was calibrated using a Si-reference cell certified by NREL before taking measurements. No light soaking was applied before the potential scan. The J-V curves were measured using a reverse scan (from a forward bias [1.2 V] to short circuit [0 V]) and a forward scan (from a forward bias [0 V] to short circuit [1.2 V]). The step voltage was fixed at 100 mV. The cells were masked using a metal mask in order to limit the active cell area to  $0.0804\text{ cm}^2$ . EQE measurements were obtained using a QEX7 system (PV Measurement). The stability test was conducted without encapsulation. The thermal stability test was performed by aging on a hot plate at RT and 40°C, respectively. The performances of the devices were periodically measured under illumination AM 1.5 G after cooling the devices to RT. The photostability test was performed under a maximum power point tracking and continuous light irradiation (AM 1.5G) at 25°C and below 30% RH.

#### Density Functional Theory Calculation

All DFT calculations were performed using the Cambridge Serial Total Energy Package (CASTEP) program.<sup>75,76</sup> The electronic exchange correlation potential was treated using a generalized gradient approximation with the Perdew-Burke-Ernzerhof (GGA-PBE) functional.<sup>77</sup> The interactions of the electron-ion cores were described using a norm-conserving pseudopotential.<sup>78</sup> The van der Waals interactions were corrected using the Tkatchenko and Scheffler (TS) method.<sup>79</sup> Spin polarization was considered in all calculations. The electronic wave functions were expanded using the plane wave basis set with the energy cut-off of 700 eV. The self-consistent field calculations were performed using the convergence criterion of  $1 \times 10^{-6}$  eV/atom. The convergence criteria for the geometry optimization were set to  $1 \times 10^{-5}$  eV/atom for the maximum energy change, 0.03 eV/Å for the maximum force, 0.05 GPa for the maximum stress, and  $1 \times 10^{-3}$  Å for the maximum displacement. The Brillouin zone was sampled using a  $1 \times 1 \times 3$  k-point set with the Monkhorst-Pack scheme<sup>80</sup> for geometry optimization. Note that for calculation of projected density of states (PDOS),  $2 \times 2 \times 6$  k-point set was used.

#### SUPPLEMENTAL INFORMATION

Supplemental Information can be found online at <https://doi.org/10.1016/j.joule.2019.06.014>.

#### ACKNOWLEDGMENTS

This work was supported by the Development Program of the Korea Institute of Energy Research (KIER) (B9-2411 and B9-2415), South Korea. S.K.K. acknowledges the financial support from the National Research Foundation of South Korea (NRF-2014R1A5A1009799) and computational resources from UNIST-HPC.

## AUTHOR CONTRIBUTIONS

S.K.K., J.Y.K., and D.S.K. designed the research. M.K., G.-H.K., and T.K.L. studied constructing the concept and characterization measurements and analyzed the data. Y.J.Y. and J.W.K. performed XPS and AFM data analysis. T.K.L. and J.L. performed computational calculations. M.K., I.W.C., H.W.C., Y.J., and D.H. performed film fabrication and spectroscopic and other characterization. H.L., S.K.K., J.Y.K., and D.S.K. suggested additional experiments and provided critical feedback and advice. M.K., G.-H.K., and T.K.L. wrote the manuscript with comments from all authors.

## DECLARATION OF INTERESTS

The authors declare no competing interests.

Received: April 10, 2019

Revised: June 5, 2019

Accepted: June 13, 2019

Published: June 21, 2019

## REFERENCES

1. Jiang, Q., Zhao, Y., Zhang, X., Yang, X., Chen, Y., Chu, Z., Ye, Q., Li, X., Yin, Z., and You, J. (2019). Surface passivation of perovskite film for efficient solar cells. *Nature Photonics*. <https://doi.org/10.1038/s41566-019-0398-2>.
2. Kim, H.-S., Mora-Sero, I., Gonzalez-Pedro, V., Fabregat-Santiago, F., Juarez-Perez, E.J., Park, N.-G., and Bisquert, J. (2013). Mechanism of carrier accumulation in perovskite thin-absorber solar cells. *Nat. Commun.* 4, 2242.
3. Wehrenfennig, C., Eperon, G.E., Johnston, M.B., Snaith, H.J., and Herz, L.M. (2014). High charge carrier mobilities and lifetimes in organolead trihalide perovskites. *Adv. Mater.* 26, 1584–1589.
4. Lee, M.M., Teuscher, J., Miyasaka, T., Murakami, T.N., and Snaith, H.J. (2012). Efficient hybrid solar cells based on meso-superstructured organometal halide perovskites. *Science* 338, 643–647.
5. Chen, Q., Marco, N.D., Yang, Y., Song, T.-B., Chen, C.-C., Zhao, H., Hong, Z., Zhou, H., and Yang, Y. (2015). Under the spotlight: The organic–inorganic hybrid halide perovskite for optoelectronic applications. *Nano Today* 10, 355–396.
6. Oga, H., Saeki, A., Ogomi, Y., Hayase, S., and Seki, S. (2014). Improved understanding of the electronic and energetic landscapes of perovskite solar cells: high local charge carrier mobility, reduced recombination, and extremely shallow traps. *J. Am. Chem. Soc.* 136, 13818–13825.
7. Zhang, W., Saliba, M., Moore, D.T., Pathak, S.K., Hörrantner, M.T., Stergiopoulos, T., Stranks, S.D., Eperon, G.E., Alexander-Webber, J.A., Abate, A., et al. (2015). Ultrasmooth organic-inorganic perovskite thin-film formation and crystallization for efficient planar heterojunction solar cells. *Nat. Commun.* 6, 6142.
8. Jacobsson, T.J., Correa-Baena, J.-P., Pazoki, M., Saliba, M., Schenk, K., Grätzel, M., and Hagfeldt, A. (2016). Exploration of the compositional space for mixed lead halogen perovskites for high efficiency solar cells. *Energy Environ. Sci.* 9, 1706–1724.
9. Weber, D. (1978).  $\text{CH}_3\text{NH}_3\text{PbX}_3$ , a Pb(II)-System with Cubic Perovskite Structure. *Z. Naturforsch. C* 33B, 1443–1445.
10. Weber, D. (1978).  $\text{CH}_3\text{NH}_3\text{SnBr}_{3-x}\text{J}_{3-x}$  ( $x = 0\text{--}3$ ), a Sn(II)-System with Cubic Perovskite Structure. *Z. Naturforsch. C* 33B, 862–865.
11. Koh, T.M., Fu, K., Fang, Y., Chen, S., Sum, T.C., Mathews, N., Mhaisalkar, S.G., Boix, P.P., and Baikie, T. (2014). Formamidinium-Containing Metal-Halide: An Alternative Material for Near-IR Absorption Perovskite Solar Cells. *J. Phys. Chem. C* 118, 16458–16462.
12. Pellet, N., Gao, P., Gregori, G., Yang, T.-Y., Nazeeruddin, M.K., Maier, J., and Grätzel, M. (2014). Mixed-Organic-Cation Perovskite Photovoltaics for Enhanced Solar-Light Harvesting. In *Angew. Chem. Int. Fifty Third Edition*, pp. 3151–3157.
13. Lee, J.-W., Seol, D.-J., Cho, A.-N., and Park, N.-G. (2014). High-efficiency perovskite solar cells based on the black polymorph of  $\text{HC}(\text{NH}_2)_2\text{PbI}_3$ . *Adv. Mater.* 26, 4991–4998.
14. Han, Q., Bae, S.-H., Sun, P., Hsieh, Y.-T., Yang, Y.-M., Rim, Y.S., Zhao, H., Chen, Q., Shi, W., Li, G., and Yang, Y. (2016). Single Crystal Formamidinium Lead Iodide ( $\text{FAPbI}_3$ ): Insight into the Structural, Optical, and Electrical Properties. *Adv. Mater.* 28, 2253–2258.
15. Heo, J.H., Song, D.H., and Im, S.H. (2014). Planar  $\text{CH}_3\text{NH}_3\text{PbBr}_3$  hybrid solar cells with 10.4% power conversion efficiency, fabricated by controlled crystallization in the spin-coating process. *Adv. Mater.* 26, 8179–8183.
16. Jeon, N.J., Noh, J.H., Kim, Y.C., Yang, W.S., Ryu, S., and Seok, S.I. (2014). Solvent engineering for high-performance inorganic–organic hybrid perovskite solar cells. *Nat. Mater.* 13, 897–903.
17. Yang, W.S., Noh, J.H., Jeon, N.J., Kim, Y.C., Ryu, S., Seo, J., and Seok, S.I. (2015). SOLAR CELLS. High-performance photovoltaic perovskite layers fabricated through intramolecular exchange. *Science* 348, 1234–1237.
18. Tu, Y., Wu, J., Lan, Z., He, X., Dong, J., Jia, J., Guo, P., Lin, J., Huang, M., and Huang, Y. (2017). Modulated  $\text{CH}_3\text{NH}_3\text{PbI}_{3-x}\text{Br}_x$  film for efficient perovskite solar cells exceeding 18%. *Sci. Rep.* 7, 44603.
19. Green, M.A., Ho-Baillie, A., and Snaith, H.J. (2014). The emergence of perovskite solar cells. *Nat. Photonics* 8, 506–514.
20. Kim, M., Kim, G.-H., Oh, K.S., Jo, Y., Yoon, H., Kim, K.-H., Lee, H., Kim, J.Y., and Kim, D.S. (2017). High-Temperature-Short-Time Annealing Process for High-Performance Large-Area Perovskite Solar Cells. *ACS Nano* 11, 6057–6064.
21. Pool, V.L., Dou, B., Van Campen, D.G., Klein-Stockert, T.R., Barnes, F.S., Shaheen, S.E., Ahmad, M.I., van Heest, M.F.A.M., and Toney, M.F. (2017). Thermal engineering of  $\text{FAPbI}_3$  perovskite material via radiative thermal annealing and *in situ* XRD. *Nat. Commun.* 8, 14075.
22. Tai, Q., You, P., Sang, H., Liu, Z., Hu, C., Chan, H.L.W., and Yan, F. (2016). Efficient and stable perovskite solar cells prepared in ambient air irrespective of the humidity. *Nat. Commun.* 7, 11105.
23. Zhao, P., Kim, B.J., and Jung, H.S. (2018). Passivation in perovskite solar cells: A review. *Materials Today Energy* 7, 267–286.
24. Li, T., Pan, Y., Wang, Z., Xia, Y., Chen, Y., and Huang, W. (2017). Additive engineering for highly efficient organic–inorganic halide perovskite solar cells: recent advances and perspectives. *J. Mater. Chem. A Mater. Energy Sustain.* 5, 12602–12652.

25. Chang, C.Y., Chu, C.Y., Huang, Y.C., Huang, C.W., Chang, S.Y., Chen, C.A., Chao, C.Y., and Su, W.F. (2015). Tuning perovskite morphology by polymer additive for high efficiency solar cell. *ACS Appl. Mater. Interfaces* 7, 4955–4961.
26. Zhao, Y., Wei, J., Li, H., Yan, Y., Zhou, W., Yu, D., and Zhao, Q. (2016). A polymer scaffold for self-healing perovskite solar cells. *Nat. Commun.* 7, 10228.
27. Guo, Y., Shoyama, K., Sato, W., and Nakamura, E. (2016). Polymer Stabilization of Lead(II) Perovskite Cubic Nanocrystals for Semitransparent Solar Cells. *Adv. Energy Mater.* 6, 1502317.
28. Chiang, C.-H., and Wu, C.-G. (2016). Bulk heterojunction perovskite–PCBM solar cells with high fill factor. *Nat. Photonics* 10, 196–200.
29. Wang, K., Liu, C., Du, P., Zheng, J., and Gong, X. (2015). Bulk heterojunction perovskite hybrid solar cells with large fill factor. *Energy Environ. Sci.* 8, 1245–1255.
30. Liu, C., Wang, K., Du, P., Yi, C., Meng, T., and Gong, X. (2015). Efficient Solution-Processed Bulk Heterojunction Perovskite Hybrid Solar Cells. *Adv. Energy Mater.* 5, 1402024.
31. Sun, C., Xue, Q., Hu, Z., Chen, Z., Huang, F., Yip, H.L., and Cao, Y. (2015). Phosphonium Halides as Both Processing Additives and Interfacial Modifiers for High Performance Planar-Heterojunction Perovskite Solar Cells. *Small* 11, 3344–3350.
32. Wang, Y., Song, N., Feng, L., and Deng, X. (2016). Effects of Organic Cation Additives on the Fast Growth of Perovskite Thin Films for Efficient Planar Heterojunction Solar Cells. *ACS Appl. Mater. Interfaces* 8, 24703–24711.
33. Zhao, Y., and Zhu, K. (2014). Efficient planar perovskite solar cells based on a 1.8 eV band gap  $\text{CH}_3\text{NH}_3\text{PbI}_2\text{Br}$  nanosheets via thermal decomposition. *J. Am. Chem. Soc.* 136, 12241–12244.
34. Mei, A., Li, X., Liu, L., Ku, Z., Liu, T., Rong, Y., Xu, M., Hu, M., Chen, J., Yang, Y., et al. (2014). A hole-conductor-free, fully printable mesoscopic perovskite solar cell with high stability. *Science* 345, 295–298.
35. Li, N., Zhu, Z., Chueh, C.-C., Liu, H., Peng, B., Petrone, A., Li, X., Wang, L., and Jen, A.-K.-Y. (2017). Mixed Cation  $\text{FA}_x\text{PEA}_{1-x}\text{PbI}_3$  with Enhanced Phase and Ambient Stability toward High-Performance Perovskite Solar Cells. *Adv. Energy Mater.* 7, 1601307.
36. Boopathi, K.M., Mohan, R., Huang, T.-Y., Budiantoro, W., Lin, M.-Y., Lee, C.-H., Ho, K.-C., and Chu, C.-W. (2016). Synergistic improvements in stability and performance of lead iodide perovskite solar cells incorporating salt additives. *J. Mater. Chem. A Mater. Energy Sustain.* 4, 1591–1597.
37. Abdi-Jalebi, M., Dar, M.I., Sadhanala, A., Senanayak, S.P., Frankevičius, M., Arora, N., Hu, Y., Nazeeruddin, M.K., Zakeeruddin, S.M., Grätzel, M., and Friend, R.H. (2016). Impact of Monovalent Cation Halide Additives on the Structural and Optoelectronic Properties of  $\text{CH}_3\text{NH}_3\text{PbI}_3$  Perovskite. *Adv. Energy Mater.* 6, 1502472.
38. Chen, Y., Zhao, Y., and Liang, Z. (2015). Nonvolatile chlorinated additives adversely influence  $\text{CH}_3\text{NH}_3\text{PbI}_3$  based planar solar cells. *J. Mater. Chem. A Mater. Energy Sustain.* 3, 9137–9140.
39. Kumar, M.H., Dharani, S., Leong, W.L., Boix, P.P., Prabhakar, R.R., Baikie, T., Shi, C., Ding, H., Ramesh, R., Asta, M., et al. (2014). Lead-free halide perovskite solar cells with high photocurrents realized through vacancy modulation. *Adv. Mater.* 26, 7122–7127.
40. Heo, J.H., Song, D.H., Han, H.J., Kim, S.Y., Kim, J.H., Kim, D., Shin, H.W., Ahn, T.K., Wolf, C., Lee, T.W., and Im, S.H. (2015). Planar  $\text{CH}_3\text{NH}_3\text{PbI}_3$  Perovskite Solar Cells with Constant 17.2% Average Power Conversion Efficiency Irrespective of the Scan Rate. *Adv. Mater.* 27, 3424–3430.
41. Lee, S.J., Shin, S.S., Kim, Y.C., Kim, D., Ahn, T.K., Noh, J.H., Seo, J., and Seok, S.I. (2016). Fabrication of Efficient Formamidinium Tin Iodide Perovskite Solar Cells through  $\text{SnF}_2$ -Pyrazine Complex. *J. Am. Chem. Soc.* 138, 3974–3977.
42. Huang, J., Wang, M., Ding, L., Yang, Z., and Zhang, K. (2016). Hydrobromic acid assisted crystallization of  $\text{MAPbI}_{3-x}\text{Cl}_x$  for enhanced power conversion efficiency in perovskite solar cells. *RSC Advances* 6, 55720–55725.
43. Bassiri-Gharb, N., Bastani, Y., and Bernal, A. (2014). Chemical solution growth of ferroelectric oxide thin films and nanostructures. *Chem. Soc. Rev.* 43, 2125–2140.
44. Chen, Y., Zhao, Y., and Liang, Z. (2015). Non-Thermal Annealing Fabrication of Efficient Planar Perovskite Solar Cells with Inclusion of  $\text{NH}_4\text{Cl}$ . *Chem. Mater.* 27, 1448–1451.
45. Qin, C., Matsushima, T., Fujihara, T., and Adachi, C. (2017). Multifunctional Benzoquinone Additive for Efficient and Stable Planar Perovskite Solar Cells. *Adv. Mater.* 29, 1603808.
46. Li, S., Chang, C.-H., Wang, Y.-C., Lin, C.-W., Wang, D.-Y., Lin, J.-C., Chen, C.-C., Sheu, H.-S., Chia, H.-C., Wu, W.-R., et al. (2016). Intermixing-seeded growth for high-performance planar heterojunction perovskite solar cells assisted by precursor-capped nanoparticles. *Energy Environ. Sci.* 9, 1282–1289.
47. Kulbak, M., Cahen, D., and Hodes, G. (2015). How Important Is the Organic Part of Lead Halide Perovskite Photovoltaic Cells? Efficient  $\text{CsPbBr}_3$  Cells. *J. Phys. Chem. Lett.* 6, 2452–2456.
48. Lee, J.-W., Kim, D.-H., Kim, H.-S., Seo, S.-W., Cho, S.M., and Park, N.-G. (2015). Formamidinium and Cesium Hybridization for Photo- and Moisture-Stable Perovskite Solar Cell. *Adv. Energy Mater.* 5, 1501310.
49. Choi, H., Jeong, J., Kim, H.-B., Kim, S., Walker, B., Kim, G.-H., and Kim, J.Y. (2014). Cesium-doped methylammonium lead iodide perovskite light absorber for hybrid solar cells. *Nano Energy* 7, 80–85.
50. Saliba, M., Matsui, T., Seo, J.-Y., Domanski, K., Correa-Baena, J.-P., Nazeeruddin, M.K., Zakeeruddin, S.M., Tress, W., Abate, A., Hagfeldt, A., and Grätzel, M. (2016). Cesium-containing triple cation perovskite solar cells: improved stability, reproducibility and high efficiency. *Energy Environ. Sci.* 9, 1989–1997.
51. Yadav, P., Dar, M.I., Arora, N., Alharbi, E.A., Giordano, F., Zakeeruddin, S.M., and Grätzel, M. (2017). The Role of Rubidium in Multiple-Cation-Based High-Efficiency Perovskite Solar Cells. *Adv. Mater.* 29, 1701077.
52. Bella, F., Griffini, G., Correa-Baena, J.-P., Saracco, G., Grätzel, M., Hagfeldt, A., Turri, S., and Gerbaldo, C. (2016). Improving efficiency and stability of perovskite solar cells with photocurable fluoropolymers. *Science* 354, 203–206.
53. Zhang, M., Yun, J.S., Ma, Q., Zheng, J., Lau, C.F.J., Deng, X., Kim, J., Kim, D., Seidel, J., Green, M.A., et al. (2017). High-Efficiency Rubidium-Incorporated Perovskite Solar Cells by Gas Quenching. *ACS Energy Lett.* 2, 438–444.
54. Jodłowski, A.D., Roldán-Carmona, C., Grancini, G., Salado, M., Ralaiarisoa, M., Ahmad, S., Koch, N., Camacho, L., de Miguel, G., and Nazeeruddin, M.K. (2017). Large guanidinium cation mixed with methylammonium in lead iodide perovskites for 19% efficient solar cells. *Nat. Energy* 2, 972–979.
55. Giorgi, G., Fujisawa, J.-I., Segawa, H., and Yamashita, K. (2015). Organic–Inorganic Hybrid Lead Iodide Perovskite Featuring Zero Dipole Moment Guanidinium Cations: A Theoretical Analysis. *J. Phys. Chem. C* 119, 4694–4701.
56. Nazarenko, O., Kotyra, M.R., Yakunin, S., Aebli, M., Rainò, G., Benin, B.M., Wörle, M., and Kovalenko, M.V. (2018). Guanidinium-Formamidinium Lead Iodide: A Layered Perovskite-Related Compound with Red Luminescence at Room Temperature. *J. Am. Chem. Soc.* 140, 3850–3853.
57. Son, D.-Y., Lee, J.-W., Choi, Y.J., Jang, I.-H., Lee, S., Yoo, P.J., Shin, H., Ahn, N., Choi, M., Kim, D., and Park, N.-G. (2016). Self-formed grain boundary healing layer for highly efficient  $\text{CH}_3\text{NH}_3\text{PbI}_3$  perovskite solar cells. *Nat. Energy* 1, 16081–16088.
58. Saladoa, M., Jodłowski, A.D., Roldán-Carmona, C., de Miguel, G., Kazim, S., Nazeeruddin, M.K., and Ahmad, S. (2018). Surface passivation of perovskite layers using heterocyclic halides: Improved photovoltaic properties and intrinsic stability. *Nano Energy* 50, 220–228.
59. Wang, F., Geng, W., Zhou, Y., Fang, H.-H., Tong, C.-J., Loi, M.A., Liu, L.-M., and Zhao, N. (2016). Phenylalkylamine Passivation of Organolead Halide Perovskites Enabling High-Efficiency and Air-Stable Photovoltaic Cells. *Adv. Mater.* 28, 9986–9992.
60. Salado, M., Fernández, M.A., Holgado, J.P., Kazim, S., Nazeeruddin, M.K., Dyson, P.J., and Ahmad, S. (2017). Towards Extending Solar Cell Lifetimes: Addition of a Fluorous Cation to Triple Cation-Based Perovskite Films. *ChemSusChem* 10, 3846–3853.
61. Deepa, M., Ramos, F.J., Shivaprasad, S.M., and Ahmad, S. (2016). Unraveling the Role of Monovalent Halides in Mixed-Halide Organic–Inorganic Perovskites. *ChemPhysChem* 17, 913–920.

62. Son, D.-Y., Kim, S.-G., Seo, J.-Y., Lee, S.-H., Shin, H., Lee, D., and Park, N.G. (2018). Universal Approach toward Hysteresis-Free Perovskite Solar Cell via Defect Engineering. *J. Am. Chem. Soc.* 140, 1358–1364.
63. Wang, Z., Zhou, Y., Pang, S., Xiao, Z., Zhang, J., Chai, W., Xu, H., Liu, Z., Padture, N.P., and Cui, G. (2015). Additive-Modulated Evolution of  $\text{HC}(\text{NH}_2)_2\text{PbI}_3$  Black Polymorph for Mesoscopic Perovskite Solar Cells. *Chem. Mater.* 27, 7149–7155.
64. Xie, F., Chen, C.-C., Wu, Y., Li, X., Cai, M., Liu, X., Yang, X., and Han, L. (2017). Vertical recrystallization for highly efficient and stable formamidinium-based inverted-structure perovskite solar cells. *Energy Environ. Sci.* 10, 1942–1949.
65. Mu, C., Pan, J., Feng, S., Li, Q., and Xu, D. (2017). Quantitative Doping of Chlorine in Formamidinium Lead Trihalide ( $\text{FAPbI}_{3-x}\text{Cl}_x$ ) for Planar Heterojunction Perovskite Solar Cells. *Adv. Energy Mater.* 7, 1601297.
66. Qing, J., Liu, X.-K., Li, M., Liu, F., Yuan, Z., Tiukalova, E., Yan, Z., Duchamp, M., Chen, S., Wang, Y., et al. (2018). Aligned and Graded Type-II Ruddlesden-Popper Perovskite Films for Efficient Solar Cells. *Adv. Energy Mater.* 8, 1800185.
67. Li, G., Zhang, T., Guo, N., Xu, F., Qian, X., and Zhao, Y. (2016). Ion-Exchange-Induced 2D-3D Conversion of  $\text{HMA}_{1-x}\text{FA}_x\text{PbI}_3\text{Cl}$  Perovskite into a High-Quality  $\text{MA}_{1-x}\text{FA}_x\text{PbI}_3$  Perovskite. *Angew. Chem. Int. Ed. Engl.* 55, 13460–13464.
68. Li, X., Bi, D., Yi, C., Décoppet, J.-D., Luo, J., Zakeeruddin, S.M., Hagfeldt, A., and Grätzel, M. (2016). A vacuum flash-assisted solution process for high-efficiency large-area perovskite solar cells. *Science* 353, 58–62.
69. Frost, J.M., Butler, K.T., Brivio, F., Hendon, C.H., van Schilfgaarde, M., and Walsh, A. (2014). Atomistic origins of high-performance in hybrid halide perovskite solar cells. *Nano Lett.* 14, 2584–2590.
70. Jeon, N.J., Noh, J.H., Yang, W.S., Kim, Y.C., Ryu, S., Seo, J., and Seok, S.I. (2015). Compositional engineering of perovskite materials for high-performance solar cells. *Nature* 517, 476–480.
71. Zhumeikov, A.A., Saidaminov, M.I., Haque, M.A., Alarousu, E., Sarmah, S.P., Murali, B., Dursun, I., Miao, X.-H., Abdelhady, A.L., Wu, T., et al. (2016). Formamidinium Lead Halide Perovskite Crystals with Unprecedented Long Carrier Dynamics and Diffusion Length. *ACS Energy Lett.* 1, 32–37.
72. Nazarenko, O., Yakunin, S., Morad, V., Cherniukh, I., and Kovalenko, M.V. (2017). Single crystals of caesium formamidinium lead halide perovskites: solution growth and gamma dosimetry. *NPG Asia Mater.* 9, e373.
73. Kern, W., and Vossen, J. (1987). Cleaning Process for Silicon Wafer. *Thin Film Processes, Chapter V* (Academic Press), p. 1.
74. Kavan, L., and Grätzel, M. (1995). Highly efficient semiconducting  $\text{TiO}_2$  photoelectrodes prepared by aerosol pyrolysis. *Electrochim. Acta* 40, 643–652.
75. Clark, S.J., Segall, M.D., Pickard, C.J., Hasnip, P.J., Probert, M.I.J., Refson, K., and Payne, M.C. (2005). First principles methods using CASTEP. *Z. Kristallogr. Cryst. Mater.* 220, 567–570.
76. Materials Studio (2018). BIOVIA Inc (San Diego, CA).
77. Perdew, J.P., Burke, K., and Ernzerhof, M. (1996). Generalized Gradient Approximation Made Simple. *Phys. Rev. Lett.* 77, 3865–3868.
78. Kleinman, L., and Bylander, D.M. (1982). Efficacious Form for Model Pseudopotentials. *Phys. Rev. Lett.* 48, 1425–1428.
79. Tkatchenko, A., and Scheffler, M. (2009). Accurate molecular van der Waals interactions from ground-state electron density and free-atom reference data. *Phys. Rev. Lett.* 102, 073005.
80. Monkhorst, H.J., and Pack, J.D. (1976). Special points for Brillouin-zone integrations. *Phys. Rev. B* 13, 5188–5192.